Compton and Rayleigh double scattering of unpolarized radiation

J. E. Fernández*
Laboratorio di Ingegneria Nucleare di Montecuccolino, Università di Bologna, via dei Colli 16, 40136 Bologna, Italy
(Received 26 April 1991)

Analytical expressions describing double-scattering intensities of the Compton and Rayleigh effects (Compton-Compton, Compton-Rayleigh, Rayleigh-Compton, and Rayleigh-Rayleigh contributions), are deduced in the framework of the transport theory for an infinitely thick sample irradiated with collimated monochromatic radiation. An orders-of-interaction solution of the integro-differential Boltzmann equation for unpolarized photons is used to separate the multiple-order terms. Interaction kernels for coherent and incoherent scattering include atomic form factors describing the effect of the electronic distribution in multielectron atoms. The total attenuation coefficient of the target takes into account, besides the mentioned scattering processes, the photoelectric effect, important in the x-ray regime. First-order Compton and Rayleigh interactions give monochromatic peaks according to the theoretical model that neglects electron motion. In contrast, Compton-Compton, Compton-Rayleigh, and Rayleigh-Compton contribute asymmetric continuous spectra whose wavelength breadths are the DuMond width and $2\lambda_C$ (λ_C is the Compton wavelength), respectively. Single- and double-scattering intensities of the Rayleigh and Compton effects are computed for pure and composite materials as a function of the excitation energy and the angular orientations of the incident and take-off beams. Since absorption in the target is considered, computations can be straightforwardly compared with experimental data and with realistic Monte Carlo simulations. The agreement is good for low excitation energies because the second-order term remains dominant in multiple scattering and bremsstrahlung emission is weaker. However, for higher excitation energies the probability of higher orders of multiple scattering increases, and they cannot be neglected. Although analytical calculations are performed up to the second order in this work, a Monte Carlo simulation is used to show the importance of higher orders in light elements.

PACS number(s): 32.80.Cy, 07.85.+n, 78.70.Ck

I. INTRODUCTION

Techniques using the inelastic scattering of x and γ rays are applied to obtain information on electron-momentum distributions in a wide range of materials [1–3]. The analysis of the energy distribution of the scattered photons—the Compton profile—cannot be performed assuming that the photons undergo only one collision before arriving at the detector because there is a substantial contribution from the photons scattered two or more times that overlaps the profile. This interference must be stripped off to obtain acceptable data.

The correction of the measured Compton profile is performed in practice by subtracting the intensity spectrum due to multiple-scattering events [4]. To this end, Monte Carlo simulations are actually preferred to analytical calculations that have failed to accurately provide the information required.

The first analytical approach to the multiple scattering of the Compton effect was introduced by Dumond [5] in 1930. He predicted that multiple scattering may affect the breadth of the single Compton line, change its structure, and distort the background until rendering unreliable the Compton shift measurements. Dumond studied the problem of the double incoherent scattering of monochromatic photons by free electrons and assumed the first scatterer in the center of a solid and homogeneous sphere, neglecting absorption. He predicted a faint line or border at a shifted position of the incident wavelength. He estimated the importance of the double scattering in 14% of the single-scattering intensity for a graphite sphere of 1 cm diameter. Williams, Pattison, and Cooper [6] extended the Dumond treatment to include the scattering from moving electrons and considered the mixed case with one elastic and one inelastic collision.

Another type of analytical method is based on a generalization of the Dumond approach. In place of the electric field it deals directly with the intensity of scattered radiation and uses the narrow-beam attenuation law in a probabilistic way to write a differential expression for the intensity. As pointed by Halonen *et al.* [4] this approach leads naturally to a Monte Carlo technique. Tanner and Epstein [7,8] examined the general case with this technique in order to determine qualitatively the effects of the sample geometry, the scattering angles, the absorption coefficients, and the shape of the scattering cross sections on the intensities of single and higher-order scattering. They described the energy profile reflected by a cylindrical sample as much of finite as of infinite radii, of finite thickness and assuming constant absorption coefficients. Braun-Keller and Epstein [9,10] proposed a generalization of this approach assimilating the problem of extracting the single Compton profile from the multiple-scattering contribution to the solution of a nonlinear operator equation.

Although the natural analytical approach to attack

problems of particle diffusion in a medium, the Boltzmann transport theory, is acknowledged as being capable of tremendous generality, curiously in this field it has been discarded because it is judged unable to separate multiple-order terms [4]. What probably happened was that transport theory was initially applied in this context with the scope of finding a full solution of the Boltzmann equation: Chandrasekhar [11] and O'Rourke [12] obtained a "first-order approximation" to the total spectral distribution of isotropically scattered radiation that, unfortunately, due to the approximation they used, led to unphysical results precluding the use of monochromatic sources; and Brockwell [13] found an approximated angular solution to the intensity equation for a slab. Anyway, none of these results was adequate for finding the contributed intensity by the individual terms of multiple scattering in an infinite-thickness target (where multiple scattering becomes important) excited with a monochromatic x-ray beam.

However, equilibrium radiative-transfer techniques are a powerful tool for the study of photon transport [14,15]. Recently, transport techniques [16–21] were successfully applied in a similar framework to study the angular and energy dependence of single-order terms due to the multiple scattering of x rays in a solid thick sample under monochromatic excitation. The method is based on an appropriate solution of the Boltzmann transport equation for photons in an infinite-thickness homogeneous specimen. The reported solution [16] is exact, independent for each order of scattering, and valid with all kinds of interactions. It is the capability for separating the contribution from different chains of interactions that make this solution particularly adequate to describe mixed collision effects in general, and with the coherent and incoherent scattering in particular. Several photon-atom processes in the x-ray regime have already been tested with this solution [17–21]. These results fulfill the accuracy requirements for (analytical) Compton profile unfolding in the formal frame of the transport theory.

In what follows we shall apply such a solution with appropriate interaction kernels describing Compton and Rayleigh photon collisions with many-electron atoms, finding analytical expressions for the intensities due to double scattering in the target. Although the precollision motion of the electrons will be not considered for the sake of simplicity, the effect of the electronic distribution in the atoms will be described by means of atomic scattering factors included in the cross sections. We shall describe the Compton-Compton, Compton-Rayleigh, Rayleigh-Compton, and Rayleigh-Rayleigh x-ray wavelength spectra as a function of the direction of emission with respect to the sample surface, and of the source beam's direction, energy, and intensity. The allowed interactions in the x-ray region are the Compton and the Rayleigh scattering and the photoelectric effect. Anomalous scattering and bremsstrahlung are neglected. Besides, we shall assume that the photon energy in the x-ray regime does not exceed the threshold for pair production.

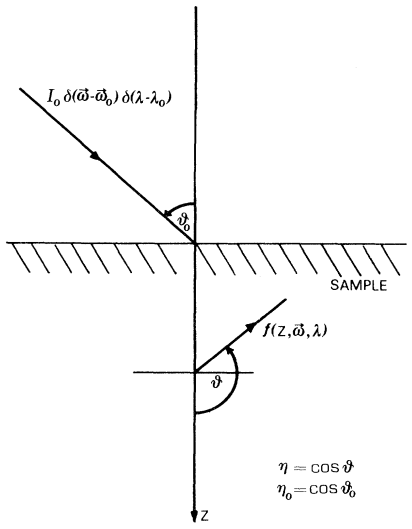

FIG. 1. Irradiation scheme of a homogeneous specimen of infinite thickness excited with a collimated monochromatic x-ray source. The magnitudes are represented in the photon transport equation (1).

We shall calculate double- to single-scattering intensity ratios as a function of the excitation-detection geometry, the incident energy, and target composition. We shall briefly discuss the influence of higher order of multiple scattering with recourse to Monte Carlo simulation.

For the sake of completeness in the following section we shall summarize theoretical results from previous papers [16,18] that will be necessary to perform our second-order intensity computations.

II. THEORY

A. Photon transport model

We consider a semi-infinite and homogeneous medium of density ρ which attenuates the incident radiation with total mass attenuation coefficient $\mu(\lambda)$. The monochromatic radiation source is plane slant monodirectional placed in the interface between the two semispaces. We are interested only in the interacting photons in the lower semispace (positive z axis). The photons crossing towards the upper side can only be absorbed in that portion of the space domain and can never return back to the sample. A sketch of the geometrical arrangement is shown in Fig. 1.

In standard notation (using $\eta=\omega_z$), the following balance equation for a source of I_0 photons per second results:

$$\eta\frac{\partial f(z,\boldsymbol{\omega},\lambda)}{\partial z}=-\mu(\lambda)f(z,\boldsymbol{\omega},\lambda)+\int_0^\infty d\lambda'\int_{4\pi}d\boldsymbol{\omega}'k(\boldsymbol{\omega},\lambda,\boldsymbol{\omega}',\lambda')\mathcal{U}(z)f(z,\boldsymbol{\omega}',\lambda')+I_0\delta(z)\delta(\boldsymbol{\omega}-\boldsymbol{\omega}_0)\delta(\lambda-\lambda_0)\ , \tag{1}$$

where $\mathcal{U}(z)$ is the unitary-step Heaviside function. The flux $f(z,\omega,\lambda)d\omega\,d\lambda$ gives the number of photons with wavelengths between λ and $\lambda+d\lambda$, and with directions between ω and $\omega+d\omega$, which cross a unit area per unit time. The wavelength λ is used in place of the energy E because it is convenient to our purposes of maintaining close compatibility with previous results in the field, but the use of E is entirely equivalent. The kernel $k(\omega,\lambda,\omega',\lambda')$ gives the probability density of photon scattering into ω and λ from ω' and λ', per unit path through the medium and per unit $d\omega$ and $d\lambda$. It contains the sum of the individual kernels for each one of the allowed processes with independent probability of occurrence. Although Eq. (1) is one dimensional, it contains the full phase-space information for the incident and take-off directions and wavelength (energy).

B. Solution of the Boltzmann equation

Equation (1) has been solved [16] by means of a Neumann-type series in powers of the kernel k. As solution we have both the source-dependent zeroth-order flux

$$f^{(0)}(z,\omega,\lambda)=\frac{I_0}{2|\eta|}\delta(\omega-\omega_0)\delta(\lambda-\lambda_0)\exp\left[-\frac{\mu|z|}{|\eta|}\right]\times(1+\mathrm{sgn}\eta\,\mathrm{sgn}z) \tag{2}$$

and the generic nth-order flux (positive z)

$$f^{(n)}(z,\omega,\lambda)=\frac{1}{|\eta|}\left[\frac{(1+\mathrm{sgn}\eta)}{2}\exp\left[-\frac{z\mu}{|\eta|}\right]\int_0^z d\tau\exp\left[\frac{\tau\mu}{|\eta|}\right]\int_0^\infty d\lambda'\int_{4\pi}d\omega' k(\omega,\lambda,\omega',\lambda')f^{(n-1)}(\tau,\omega',\lambda')\right.$$
$$\left.+\frac{(1-\mathrm{sgn}\eta)}{2}\int_0^\infty d\tau\exp\left[-\frac{\tau\mu}{|\eta|}\right]\int_0^\infty d\lambda'\int_{4\pi}d\omega' k(\omega,\lambda,\omega',\lambda')f^{(n-1)}(\tau+z,\omega',\lambda')\right], \tag{3}$$

which depends on the $(n-1)$th-order flux. The $\mathrm{sgn}\eta$ function is $+1$ or -1 according to the sign of the polar angle cosine.

The partial intensity, defined as the number of photons passing through a surface element per unit time, can be obtained as the partial current of the flux through the surface at $z=0$ (albedo flux) in the given direction. Therefore it is given by the positive-definite quantity

$$I^{(n)}(\omega,\lambda)=|\eta|f^{(n)}(0,\omega,\lambda)\ . \tag{4}$$

The partial intensity $I^{(n)}$ gives the number of photons (of order nth) by unit time, unit surface, unit solid angle, and unit wavelength, having angular direction ω and wavelength λ, and therefore offers full information about the angular and spectral properties of the emitted radiation. In a similar way we define the wavelength-integrated intensity

$$\mathcal{J}^{(n)}(\omega)=\int_0^\infty d\lambda\, I^{(n)}(\omega,\lambda) \tag{5}$$

that totals the spectral information and gives the magnitude of the whole partial intensity emitted in the direction ω.

The first-order intensity is obtained straightforwardly by replacing Eq. (3) (with $n=1$) in Eq. (4). An explicit relationship [18] for the second-order intensity was derived for the couple of interactions a and b (in this order)

$$I_{ab}^{(2)}(\omega,\lambda)=\frac{1-\mathrm{sgn}\eta}{2}\frac{1+\mathrm{sgn}\eta_0}{2}\frac{I_0}{|\eta_0|}\frac{1}{\mu/|\eta|+\mu_0/|\eta_0|}$$
$$\times\int_0^\infty d\lambda'\int_{4\pi}d\omega' k_b(\omega,\lambda,\omega',\lambda')k_a(\omega',\lambda',\omega_0,\lambda_0)\frac{1}{|\eta'|}$$
$$\times\left[\frac{1+\mathrm{sgn}\eta'}{2}\frac{1}{\mu/|\eta|+\mu'/|\eta'|}+\frac{1-\mathrm{sgn}\eta'}{2}\frac{1}{\mu_0/|\eta_0|+\mu'/|\eta'|}\right]. \tag{6}$$

C. Photon interactions dominating the x-ray regime

Equation (6) is valid with the class of photon-atom interactions producing a secondary photon, therefore able to be considered as photon-photon interactions. What is named an interaction may not be strictly a single process. Any sequence of physical processes in rapid succession started by a photon and that produces an end photon can be considered as a unique interaction from this point of view. The obvious drawback of this approach is the missing photons produced by the particles (other than photons) freed during the photon-atom interactions. In considering such a contribution the transport problem becomes far more complicated. In order to add the photons originated by electron interactions, for example, it is necessary to handle two coupled transport equations, one for photons and the other for electrons, and certainly the transport of charged particles is not to be solved analytically. Anyway, the error of ignoring the class of particle-photon interactions will depend on their relative

probability to the competing photon-photon processes. In this work we shall assume that the main interactions between photons and isolated atoms giving place to secondary photons are the coherent and the incoherent scattering and the photoelectric effect [22,23]. We shall neglect other possible photon sources [24,25] and, particularly, the anomalous scattering [26], the pair production-annihilation and the bremsstrahlung of photoelectric and Compton electrons [27]. These assumptions are good enough within the energy range between 1 and 100 keV.

The possible processes of double scattering involving the three interactions allowed in this work are shown in Table I, together with some references about their study with this transport model.

The single-process kernels play an important role in Eq. (6) because they represent the probability density—by unit wavelength, by unit solid angle, and by unit path—that the process may change the phase-space variables from (ω',λ') to (ω,λ). Therefore a kernel is directly related to the double-differential scattering coefficient of the interaction. Thus the scattering coefficient for the process T can be obtained from

$$\sigma_T(\lambda',\omega')=\int_0^\infty d\lambda \int_{4\pi} d\omega\, k_T(\omega,\lambda,\omega',\lambda') , \tag{7}$$

allowing the comparison with experimental or theoretical data. Since the three photon-photon processes that we are considering are statistically independent and since they constitute the main part of the total attenuation coefficient as can be appreciated even in the most recent compilations [28], we can define the total attenuation coefficient as

$$\mu=\sigma_C+\sigma_R+\tau , \tag{8}$$

where σ_C and σ_R are the Compton (incoherent) and Rayleigh (coherent) integral attenuation coefficients and τ is the photoelectric attenuation coefficient.

In what follows we shall write the interaction kernels for the scattering processes of interest in this work. Since our aim is to explain the contribution of the multiple-scattering terms, we shall use coherent and incoherent scattering factors to describe atomic modification (electron binding and electronic charge distribution) of the single-electron-scattering cross sections. The form-factor approximation associates a smooth behavior with the scattering cross sections that cannot explain scattering resonances, but it gives a quite detailed view of the atomic effects on the scattering of photons. On the other hand, we shall not consider the motion of the electrons in the atom which could complicate the transport equation. However, at least for the incoherent case, the scattering factor can be obtained from the integration through momentum profiles of single orbitals [29] giving a simple connection between the Compton profiles and the corresponding scattering factor. Polarization effects are outside the scope of this work.

1. *Coherent (Rayleigh) scattering kernel*

The coherent scattering is a process where the photons change direction but not energy. This scattering takes place with the more bound electrons of the atom which behave rigidly during the interaction. The Rayleigh atomic kernel for unpolarized photons, with phase-space coordinates (ω',λ') scattered by a pure element target with atomic number Z into the coordinates (ω,λ), is [18]

$$k_R(\omega,\lambda,\omega',\lambda')=\sigma\delta(\lambda-\lambda')[1+(\omega\cdot\omega')^2] \times\frac{F^2(\lambda',\omega\cdot\omega',Z)}{Z} , \tag{9}$$

where $\sigma=\rho NZr_0^2/(2A)$ is a macroscopic scattering coefficient (in cm^{-1}), r_0 being the classical radius of the electron, N Avogadro's number, ρ the density, and A the atomic weight. The δ function stresses the monochroma-

TABLE I. Physical meaning of the double-scattering chains (a,b) involving the photoelectric effect, and Rayleigh and Compton scattering. Only the Rayleigh and Compton interaction effects are analyzed in this work. XRF denotes x-ray fluorescence.

a \ b	Photoelectric effect	Coherent scattering (Rayleigh)	Incoherent scattering (Compton)
Photoelectric effect	Secondary XRF intensity. Eq. (13b) in Ref. [17].	XRF photons Rayleigh scattered towards the detector. Discrete spectrum Eq. (13) in [20].	XRF photons Compton scattered towards the detector. Continuous spectrum. Modifies the XRF line shape Eq. (16) in [20].
Coherent scattering (Rayleigh)	XRF due to photoelectric absorption of Rayleigh scattering. Discrete spectrum. Eq. (12) in [20].	Discrete spectrum. Eq. (15).	Continuous spectrum. Modifies the Compton peak. Eq. (26).
Incoherent scattering (Compton)	XRF due to photoelectric absorption of Compton scattering. Discrete spectrum. Eq. (14) in [20].	Continuous spectrum Modifies the Compton peak. Eq. (28).	Continuous spectrum Modifies the Compton peak Eq. (24).

ticity of the scattering. The angular dependence of the kernel (9) is given by the last two factors: the Thomson angular factor, and the atomic form factor comprising the constructive interference from the whole atomic charge distribution. The coherent form factor $F(\lambda',\boldsymbol{\omega}\cdot\boldsymbol{\omega}',Z)$ can explain atomic contributions that are significantly greater than Z times the contribution from one single electron. Special limits are $F(\lambda',1,Z)=F(\infty,\boldsymbol{\omega}\cdot\boldsymbol{\omega}',Z)=Z$ and $F(0,\boldsymbol{\omega}\cdot\boldsymbol{\omega}',Z)=0$. Experimental data tables of form factors and references to theoretical computations for many-electron atoms may be found in the classic paper of Hubbell *et al.* [30] and in more recent works [31,32]. A closed expression [33] giving approximated values for F is available. More precise values are achieved with semiempirical formulas and fitting coefficients of theoretical calculations [34].

2. *Incoherent (Compton) scattering kernel*

In incoherent scattering, energy as well as direction is changed. This process takes place with the outer electrons of the atom. The Compton atomic kernel for incident photons, with phase-space coordinates $(\boldsymbol{\omega}',\lambda')$ scattered by a pure element target of atomic number Z into the coordinates $(\boldsymbol{\omega},\lambda)$, is [18]

$$k_C(\boldsymbol{\omega},\lambda,\boldsymbol{\omega}',\lambda')=\sigma K_{\mathrm{KN}}(\lambda,\lambda')S(\lambda',\boldsymbol{\omega}\cdot\boldsymbol{\omega}',Z)\frac{1}{\lambda_C}\times\delta\left[1-\boldsymbol{\omega}\cdot\boldsymbol{\omega}'+\frac{\lambda'-\lambda}{\lambda_C}\right], \tag{10}$$

where

$$K_{\mathrm{KN}}(\lambda,\lambda')=\left[\frac{\lambda'}{\lambda}\right]^2\left[\frac{\lambda}{\lambda'}+\frac{\lambda'}{\lambda}+\frac{\lambda-\lambda'}{\lambda_C}\left[\frac{\lambda-\lambda'}{\lambda_C}-2\right]\right] \tag{11}$$

and $\lambda_C=0.0242$ Å is the Compton wavelength. The $\sigma K_{\mathrm{KN}}(\lambda,\lambda')$ factor denotes the well-known Klein-Nishina differential coefficient [25,35]. The direction-wavelength δ fixes the integration path in the phase space along the line $1-\boldsymbol{\omega}\cdot\boldsymbol{\omega}'+(\lambda'-\lambda)/\lambda_C=0$ (this condition does not account for the shift for bound electrons [36]). $S(\lambda',\boldsymbol{\omega}\cdot\boldsymbol{\omega}',Z)$ is an incoherent scattering form factor taking into account the electron binding. Some special limits are $S(\lambda',1,Z)=S(\infty,\boldsymbol{\omega}\cdot\boldsymbol{\omega}',Z)=0$ and $S(0,\boldsymbol{\omega}\cdot\boldsymbol{\omega}',Z)=1$. Data tables and references to theoretical computations are found elsewhere [30,32] (note that the "scattering function" in Ref. [30] means SZ here). A closed-form approximation formula for S was obtained [33] with the Thomas-Fermi model. Precise values of the S factor can be computed with semiempirical formulas and fitting coefficients to theoretical calculations [37].

The precollision motion of the electrons has been ignored in the kernel (10), limiting the Compton peak to a monochromatic line. The more rigorous theoretical treatment associated with the Compton profile is not sufficiently tractable for extensive calculation and will not be considered here. However, the multiple-scattering effects will be better appreciated in a context of generality, independent of the state of excitation of the atom and the chemical bond to other atoms.

III. MULTIPLE SCATTERING OF THE RAYLEIGH AND COMPTON EFFECTS

A. Rayleigh and Compton peaks

The first-order intensities describing the emission of photons due to one single Rayleigh or Compton scattering into a pure element target are given, respectively, by

$$I_R^{(1)}(\boldsymbol{\omega},\lambda)=\delta(\lambda-\lambda_0)\frac{\sigma}{Z}A(\eta_0,\lambda_0,\eta,\lambda_0)[1+(\boldsymbol{\omega}\cdot\boldsymbol{\omega}_0)^2]F^2(\lambda_0,\boldsymbol{\omega}\cdot\boldsymbol{\omega}_0,Z)\,, \tag{12}$$

$$I_C^{(1)}(\omega,\lambda)=\delta(\lambda_0+\lambda_C(1-\boldsymbol{\omega}\cdot\boldsymbol{\omega}_0)-\lambda)\sigma K_{\mathrm{KN}}(\lambda_0+\lambda_C(1-\boldsymbol{\omega}\cdot\boldsymbol{\omega}_0),\lambda_0)A(\eta_0,\lambda_0,\eta,\lambda_0+\lambda_C(1-\boldsymbol{\omega}\cdot\boldsymbol{\omega}_0))S(\lambda_0,\boldsymbol{\omega}\cdot\boldsymbol{\omega}_0,Z)\,, \tag{13}$$

where

$$A(\eta_1,\lambda_1,\eta_2,\lambda_2)=\frac{1-\mathrm{sgn}\eta_2}{2}\frac{1+\mathrm{sgn}\eta_1}{2}\frac{I_0}{|\eta_1|}\frac{1}{\mu(\lambda_1)/|\eta_1|+\mu(\lambda_2)/|\eta_2|}\,. \tag{14}$$

Equations (12) and (13) represent, respectively, the intensities of the Rayleigh and Compton peaks. Since we neglected the motion of the electrons both peaks are monochromatic for the source and geometry considered.

B. Chains of double scattering involving the Rayleigh and Compton effects

There are four contributions involving a double scattering with the Rayleigh and the Compton effects: Rayleigh-Rayleigh, Compton-Compton, Compton-Rayleigh, and Rayleigh-Compton. The mathematical complexity in the computation of these intensities depends on whether the involved scattering is Rayleigh or Compton. The Rayleigh-scattering contributions are discrete and do not change the energy of the incident radiation. The intensities contributed by the Compton effect depend on the coupled relationship between the scattering angle cosine and the wavelength shift which introduces some difficulties in the computation with these processes. The coupling between wavelength and direction prevents the separation of the phase-space integrals and make it necessary to separate them with mathematical tricks.

1. *Rayleigh-Rayleigh contribution*

This contribution can be easily calculated due to the monochromatic kernel of the Rayleigh scattering. By replacing both kernels k_a and k_b by k_R in Eq. (6) the intensity can be straightforwardly expressed as

$$I^2_{(\text{Rayleigh-Rayleigh})}(\omega,\lambda)=\delta(\lambda-\lambda_0)\left[\frac{\sigma}{Z}\right]^2 A(\eta_0,\lambda_0,\eta,\lambda_0)$$
$$\times\left[\int_0^{2\pi}d\varphi'\int_0^1 d\eta'\frac{1}{\eta'}\frac{[1+(\omega'\cdot\omega^{(+)})^2][1+(\omega'\cdot\omega_0^{(+)})^2]}{\mu_0/|\eta|+\mu_0/\eta'}F^2(\lambda_0,\omega'\cdot\omega^{(+)},Z)F^2(\lambda_0,\omega'\cdot\omega_0^{(+)},Z)\right.$$
$$\left.+\int_0^{2\pi}d\varphi'\int_0^1 d\eta'\frac{1}{\eta'}\frac{[1+(\omega'\cdot\omega^{(-)})^2][1+(\omega'\cdot\omega_0^{(-)})^2]}{\mu_0/|\eta|+\mu_0/\eta'}F^2(\lambda_0,\omega'\cdot\omega^{(-)},Z)F^2(\lambda_0,\omega'\cdot\omega_0^{(-)},Z)\right], \tag{15}$$

where

$$\omega'\cdot\omega_0^{(\pm)}=\pm\eta'\eta_0+(1-\eta'^2)^{1/2}(1-\eta_0^2)^{1/2}\cos(\varphi'-\varphi_0)\ , \tag{16a}$$
$$\omega\cdot\omega^{(\pm)}=\pm\eta'\eta+(1-\eta'^2)^{1/2}(1-\eta^2)^{1/2}\cos(\varphi'-\varphi)\ . \tag{16b}$$

Equation (15) gives the Rayleigh-Rayleigh discrete modification to the coherent line (12).

2. *Compton-Compton contribution*

The double scattering of the Compton effect is not so straightforward as the Rayleigh one. Substitution of both kernels, a and b, by the Compton kernel (10) in Eq. (6) gives

$$I^{(2)}_{\text{Compton-Compton}}(\omega,\lambda)=\sigma^2 A(\eta_0,\lambda_0,\eta,\lambda)$$
$$\times\int_0^\infty d\lambda'\int_{4\pi}d\omega' K_{\text{KN}}(\lambda,\lambda')K_{\text{KN}}(\lambda',\lambda_0)S(\lambda',\omega\cdot\omega',Z)S(\lambda_0,\omega_0\cdot\omega',Z)$$
$$\times\delta(\lambda_C(1-\omega\cdot\omega')+\lambda'-\lambda)\delta(\lambda_C(1-\omega_0\cdot\omega')+\lambda_0-\lambda')\frac{1}{|\eta'|}$$
$$\times\left[\frac{1+\text{sgn}\eta'}{2}\frac{1}{\mu/|\eta|+\mu'/|\eta'|}+\frac{1-\text{sgn}\eta'}{2}\frac{1}{\mu_0/|\eta_0|+\mu'/|\eta'|}\right]. \tag{17}$$

Each one of the two δ functions in Eq. (17) describes separately the integration path corresponding to one single interaction. These paths are shown in the upper part of Fig. 2. Since the vector ω' moves in all the space, both paths might separately attain a wavelength amplitude of $2\lambda_C$. However, when they are joined in the integral (17) the resulting wavelength amplitude is lower (in general) than the addition of the independent amplitudes. By applying a δ-function property it is possible to join them into a composite path of amplitude $2\lambda_C\omega_R$, where

$$\omega_R=|\omega+\omega_0|=\sqrt{2(1+\omega\cdot\omega_0)}=2\cos\frac{\chi}{2} \tag{18}$$

is the modulus of the resultant vector of the incident and the outgoing directions, and χ is the scattering angle. Since ω and ω_0 are unitary vectors, ω_R belongs to the interval [0,2]. The wavelength amplitude in the joined path is centered in $\lambda_0+2\lambda_C$ (see the lower part of Fig. 2), and it may attain the extreme values $\lambda_0+\lambda_C(2\pm\omega_R)$. It is clear that the incident and the outgoing directions define the range of the continuous spectrum. Integrating Eq. (17) over λ' and writing explicitly the angular integral we get (for $\omega_R\neq 0$)

$$I^{(2)}_{\text{Compton-Compton}}(\omega,\lambda)=\frac{\sigma^2}{\omega_R\lambda_C}A(\eta_0,\lambda_0,\eta,\lambda)$$
$$\times\int_0^{2\pi}d\varphi'\int_{-1}^1 d\eta'\frac{1}{|\eta'|}K_{\text{KN}}(\lambda,\tilde{\lambda})K_{\text{KN}}(\tilde{\lambda},\lambda_0)S(\tilde{\lambda},\omega\cdot\omega',Z)S(\lambda_0,\omega_0\cdot\omega',Z)$$
$$\times\delta(\alpha-\eta'\eta_R-(1-\eta'^2)^{1/2}(1-\eta_R^2)^{1/2}\cos\Delta)$$
$$\times\left[\frac{1+\text{sgn}\eta'}{2}\frac{1}{\mu/|\eta|+\tilde{\mu}/|\eta'|}+\frac{1-\text{sgn}\eta'}{2}\frac{1}{\mu_0/|\eta_0|+\tilde{\mu}/|\eta'|}\right], \tag{19}$$

where

$$\alpha=\frac{1}{\omega_R}\left[2+\frac{\lambda_0-\lambda}{\lambda_C}\right], \tag{20a}$$

$$\Delta=\varphi'-\varphi_R, \tag{20b}$$

$$\eta_R=\frac{\eta+\eta_0}{\omega_R}, \tag{20c}$$

$$\varphi_R=\arccos\left[\frac{(1-\eta_0^2)^{1/2}+(1-\eta^2)^{1/2}\cos\varphi}{[\omega_R^2-(\eta_0-\eta)^2]^{1/2}}\right], \tag{20d}$$

$$\tilde{\mu}\equiv\mu(\tilde{\lambda}), \tag{20e}$$

$$\tilde{\lambda}=\lambda_0+\lambda_C(1-\boldsymbol{\omega}_0\cdot\boldsymbol{\omega}'), \tag{20f}$$

and

$$\boldsymbol{\omega}_i\cdot\boldsymbol{\omega}'=\omega_i\omega'[\eta'\eta_i+(1-\eta'^2)^{1/2}(1-\eta_i^2)^{1/2}\cos(\varphi'-\varphi_i)], \tag{20g}$$

where $\boldsymbol{\omega}_i$ stands for $\boldsymbol{\omega}$, $\boldsymbol{\omega}_0$, or $\boldsymbol{\omega}_R$.

By recourse to the property

$$\delta(g(x))=\sum_n\frac{\delta(x-x_n)}{|g'(x_n)|} \quad \text{for } g(x_n)=0 \text{ and } g'(x_n)\neq 0 \tag{21}$$

the δ function of Eq. (19) transforms to

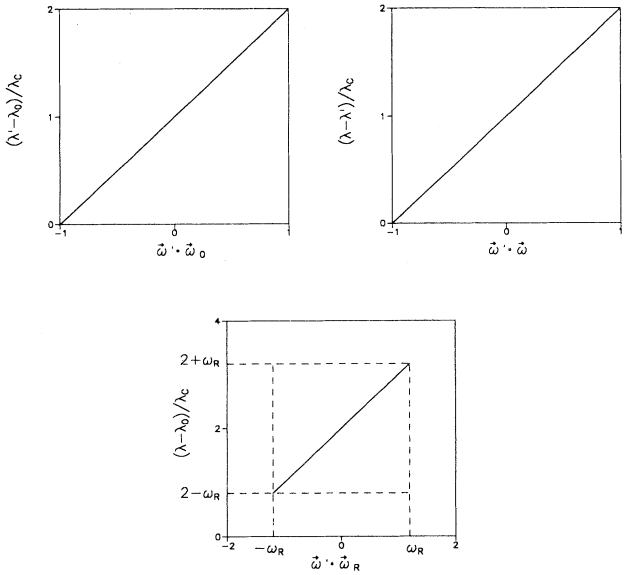

FIG. 2. Integral paths in the calculation of the Compton-Compton intensity. The upper two paths correspond to the δ functions in Eq. (17) and represent the possible wavelength changes in each isolated scattering depending on the geometry with which the interaction occurs. A chain of two interactions imposes some restrictions on the geometry of the single interactions that results in a limitation of the wavelength spectrum, as shown in the lower path. The projection of the integration angular vector $\boldsymbol{\omega}'$ on the resultant $\boldsymbol{\omega}_R$ may vary between the two symmetrical limits $\pm\omega_R$ belonging to the interval $[-2,2]$. The change in wavelength is bound by the limits $\lambda_0+\lambda_C(2\pm\omega_R)$ that belong to the interval $[\lambda_0,\lambda_0+4\lambda_C]$.

$$\frac{\delta(\varphi'-\varphi_1')+\delta(\varphi'-\varphi_2')}{[(1-\eta'^2)(1-\eta_R^2)-(\alpha-\eta'\eta_R)^2]^{1/2}}[\mathcal{U}(\eta'-\{\alpha\eta_R-[(1-\eta_R^2)(1-\alpha^2)]^{1/2}\})-\mathcal{U}(\eta'-\{\alpha\eta_R+[(1-\eta_R^2)(1-\alpha^2)]^{1/2}\})], \tag{22}$$

where

$$\varphi_1'=\varphi_R+\arccos\left[\frac{\alpha-\eta'\eta_R}{[(1-\eta'^2)(1-\eta_R^2)]^{1/2}}\right], \tag{23a}$$

and

$$\varphi_2'=2\pi+\varphi_R-(\varphi_1'-\varphi_R). \tag{23b}$$

The difference of the step functions gives the validity range of η' according to the path set by the δ function. To obtain Eq. (22) it was assumed that $\alpha^2\neq 1$ and $\eta_R^2\neq 1$.

By replacing Eq. (22) in Eq. (19) we get the final expression for the Compton-Compton intensity

$$I^{(2)}_{\text{Compton-Compton}}(\omega,\lambda)=\frac{\sigma^2}{\omega_R\lambda_C}A(\eta_0,\lambda_0,\eta,\lambda)$$

$$\times\left[\int_{\beta_1}^{\gamma_1}d\eta'\frac{1}{\eta'}\frac{\mathcal{U}(\gamma_1-\beta_1)}{[(1-\eta'^2)(1-\eta_R^2)-(\alpha-\eta'\eta_R)^2]^{1/2}}\right.$$

$$\times\sum_{k=1}^{2}\frac{K_{\text{KN}}(\lambda,\tilde{\lambda}_k^{(+)})K_{\text{KN}}(\tilde{\lambda}_k^{(+)},\lambda_0)}{\mu/|\eta|+\mu(\tilde{\lambda}_k^{(+)})/\eta'}S(\tilde{\lambda}_k^{(+)},\omega\cdot\omega_k'^{(+)},Z)S(\lambda_0,\omega_0\cdot\omega_k'^{(+)},Z)$$

$$+\int_{\beta_2}^{\gamma_2}d\eta'\frac{1}{\eta'}\frac{\mathcal{U}(\gamma_2-\beta_2)}{[(1-\eta'^2)(1-\eta_R^2)-(\alpha+\eta'\eta_R)^2]^{1/2}}$$

$$\left.\times\sum_{k=1}^{2}\frac{K_{\text{KN}}(\lambda,\tilde{\lambda}_k^{(-)})K_{\text{KN}}(\tilde{\lambda}_k^{(-)},\lambda_0)}{\mu/|\eta|+\mu(\tilde{\lambda}_k^{(-)})/\eta'}S(\tilde{\lambda}_k^{(-)},\omega\cdot\omega_k'^{(-)},Z)S(\lambda_0,\omega_0\cdot\omega_k'^{(-)},Z)\right], \tag{24}$$

where for convenience we have introduced $\beta_1=\max(0,\alpha\eta_R-D)$, $\gamma_1=\min(1,\alpha\eta_R+D)$, $\beta_2=-\min(0,\alpha\eta_R+D)$, $\gamma_2=-\max(-1,\alpha\eta_R-D)$, and the quantities

$$\omega_0\cdot\omega_k'^{(\pm)}=\pm\eta'\eta_0+(1-\eta'^2)^{1/2}(1-\eta_0^2)^{1/2}\cos(\varphi_k'^{(\pm)}-\varphi_0)\ , \tag{25a}$$

$$\omega\cdot\omega_k'^{(\pm)}=\pm\eta'\eta+(1-\eta'^2)^{1/2}(1-\eta^2)^{1/2}\cos(\varphi_k'^{(\pm)}-\varphi)\ , \tag{25b}$$

$$\varphi_1'^{(\pm)}=\varphi_R+\arccos\left[\frac{\alpha\mp\eta'\eta_R}{[(1-\eta'^2)(1-\eta_R^2)]^{1/2}}\right], \tag{25c}$$

$$\varphi_2'^{(\pm)}=2\pi+\varphi_R-(\varphi_1'^{(\pm)}-\varphi_R)\ , \tag{25d}$$

$$\tilde{\lambda}_k^{(\pm)}=\lambda_0+\lambda_C(1-\omega_0\cdot\omega_k'^{(\pm)})\ , \tag{25e}$$

$$D=[(1-\eta_R^2)(1-\alpha^2)]^{1/2}\ . \tag{25f}$$

The integration limits β_i and γ_i cannot exceed the values -1 and 1. The Heaviside functions in the integrals are different from zero only when $\gamma_i>\beta_i$ and indicate the validity range of every integral. The Compton-Compton intensity is continuous, in contrast to the preceding contribution. Its wavelength spectrum extends from $\lambda_0+\lambda_C(2-\omega_R)$ to $\lambda_0+\lambda_C(2+\omega_R)$ and has the characteristic shape shown in Fig. 3. Limit cases for special values of ω_R, η_R, and α can be calculated similarly.

3. *Rayleigh-Compton contribution*

The Compton scattering in the ω direction of Rayleigh-scattered photons is obtained replacing the kernels k_a and k_b with k_C and k_R, respectively, in Eq. (6). In a similar way as with Eq. (24), we can obtain the Rayleigh-Compton intensity

$$I^{(2)}_{\text{Rayleigh-Compton}}(\omega,\lambda)=\frac{\sigma^2}{Z\lambda_C}A(\eta_0,\lambda_0,\eta,\lambda)K_{\text{KN}}(\lambda,\lambda_0)S(\lambda_0,a,Z)$$

$$\times\left[\int_{\beta_1}^{\gamma_1}d\eta'\frac{1}{\eta'}\frac{1}{\mu/|\eta|+\mu_0/\eta'}\frac{\mathcal{U}(\gamma_1-\beta_1)}{[(1-\eta'^2)(1-\eta^2)-(a-\eta'\eta)^2]^{1/2}}\right.$$

$$\times\sum_{k=1}^{2}[1+(\omega_0\cdot\omega_k'^{(+)})^2]F^2(\lambda_0,\omega_0\cdot\omega_k'^{(+)},Z)$$

$$+\int_{\beta_2}^{\gamma_2}d\eta'\frac{1}{\eta'}\frac{1}{\mu_0/|\eta_0|+\mu_0/\eta'}\frac{\mathcal{U}(\gamma_2-\beta_2)}{[(1-\eta'^2)(1-\eta^2)-(a+\eta'\eta)^2]^{1/2}}$$

$$\left.\times\sum_{k=1}^{2}[1+(\omega_0\cdot\omega_k'^{(-)})^2]F^2(\lambda_0,\omega_0\cdot\omega_k'^{(-)},Z)\right], \tag{26}$$

where $\beta_1=\max(0,a\eta-D)$, $\gamma_1=\min(1,a\eta+D)$, $\beta_2=-\min(0,a\eta+D)$, $\gamma_2=-\max(-1,a\eta-D)$, and $\omega_0\cdot\omega_k'^{(\pm)}$—as in Eq. (25a)—are defined in terms of

$$a=1+\frac{\lambda_0-\lambda}{\lambda_C}\ , \tag{27a}$$

$$D=[(1-\eta^2)(1-a^2)]^{1/2}\ , \tag{27b}$$

$$\varphi_1'^{(\pm)}=\varphi+\arccos\left[\frac{a\mp\eta'\eta}{[(1-\eta'^2)(1-\eta^2)]^{1/2}}\right]\ , \tag{27c}$$

and

$$\varphi_2'^{(\pm)}=2\pi+\varphi-(\varphi_1'^{(\pm)}-\varphi)\ . \tag{27d}$$

The meaning of the limits β_i and γ_i is as in Eq. (24). The Rayleigh-Compton intensity is continuous and its wavelength spectrum extends from λ_0 to $\lambda_0+2\lambda_C$ (in energy from $E_0/[1+2E_0/(m_0c^2)]$ to E_0); therefore it overlaps the Compton-Compton spectrum. The shape of the Rayleigh-Compton spectrum is shown in Fig. 3. The characteristic maximum at the same energy of the Compton line broadens that peak.

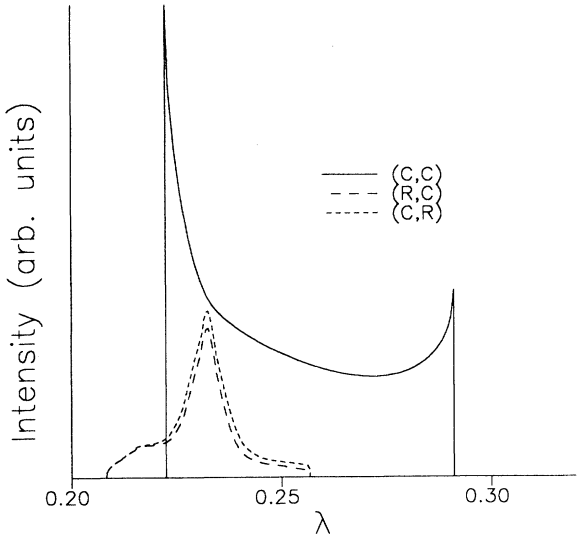

FIG. 3. Characteristic shape of the double-scattering continuous contributions due to the combined influence of the Compton and Rayleigh effects. Calculations are for Al excited with 59.54 keV (γ line of ^{241}Am) and for the geometry defined by the incidence and take-off polar angles $\vartheta_0=45°$ and $\vartheta=135°$. Azimuthal angles φ_0 and φ will be assumed as 0° unless expressly indicated.

4. *Compton-Rayleigh contribution*

The Rayleigh scattering in the ω direction of previously Compton-scattered photons is obtained similarly,

$$I^{(2)}_{\text{Compton-Rayleigh}}(\omega,\lambda)=\frac{\sigma^2}{Z\lambda_C}A(\eta_0,\lambda_0,\eta,\lambda)K_{\text{KN}}(\lambda,\lambda_0)S(\lambda_0,a,Z)$$
$$\times\left[\int_{\beta_1}^{\gamma_1}d\eta'\frac{1}{\eta'}\frac{1}{\mu/|\eta|+\mu/\eta'}\frac{\mathcal{U}(\gamma_1-\beta_1)}{[(1-\eta'^2)(1-\eta_0^2)-(a-\eta'\eta_0)^2]^{1/2}}\right.$$
$$\times\sum_{k=1}^{2}[1+(\omega\cdot\omega_k'^{(+)})^2]F^2(\lambda,\omega\cdot\omega_k'^{(+)},Z)$$
$$+\int_{\beta_2}^{\gamma_2}d\eta'\frac{1}{\eta'}\frac{1}{\mu_0/|\eta_0|+\mu/\eta'}\frac{\mathcal{U}(\gamma_2-\beta_2)}{[(1-\eta'^2)(1-\eta_0^2)-(a+\eta'\eta_0)^2]^{1/2}}$$
$$\left.\times\sum_{k=1}^{2}[1+(\omega\cdot\omega_k'^{(-)})^2]F^2(\lambda,\omega\cdot\omega_k'^{(-)},Z)\right]\ , \tag{28}$$

where $\beta_1=\max(0,a\eta_0-D)$, $\gamma_1=\min(1,a\eta_0+D)$, $\beta_2=-\min(0,a\eta_0+D)$, $\gamma_2=-\max(-1,a\eta_0-D)$, and $\omega\cdot\omega_k'^{(\pm)}$—as in Eq. (25b)—are defined in terms of

$$a=1+\frac{\lambda_0-\lambda}{\lambda_C}\ , \tag{29a}$$

$$D=[(1-\eta_0^2)(1-a^2)]^{1/2}\ , \tag{29b}$$

$$\varphi_1'^{(\pm)}=\varphi_0+\arccos\left[\frac{a\mp\eta'\eta_0}{[(1-\eta'^2)(1-\eta_0^2)]^{1/2}}\right]\ , \tag{29c}$$

and

$$\varphi_2'^{(\pm)}=2\pi+\varphi_0-(\varphi_1'^{(\pm)}-\varphi_0)\ . \tag{29d}$$

The meaning of the limits β_i and γ_i is as in the preceding equation. The Compton-Rayleigh intensity is continuous and its wavelength spectrum extends from λ_0 to $\lambda_0+2\lambda_C$ (as in the preceding case). Therefore it overlaps the Compton-Compton and the Rayleigh-Compton spectra. The shape of the Compton-Rayleigh spectrum is similar but not equal to that of Rayleigh-Compton as shown in Fig. 3.

IV. SUM RULE FOR COMPOSITE MATERIALS

The intensities contributed by double scattering, Eqs. (15), (24), (26), and (28), were deduced for a pure element

target of atomic number Z. In what follows we shall build an adequate expression valid for a mixture of several elements.

We denote with W_j the weight fraction of the element j which satisfies the relationship

$$\sum_j W_j = 1 \ . \tag{30}$$

The mass attenuation coefficient (in cm^2/g) for a composite material obeys the relation

$$\frac{\mu}{\rho} = \sum_j W_j \left[\frac{\mu}{\rho} \right]_j , \tag{31}$$

where $(\mu/\rho)_j$ is the mass attenuation coefficient for the single element j. The coefficients of the partial interactions follow similar relationships.

The intensity from a composite material is easily obtained from the intensities of the single components if we replace all the attenuation coefficients by mass attenuation coefficients in Eqs. (15), (24), (26), and (28). The following relationship stands for the intensity contributed by the double interaction chain (a,b) in a multielement target:

$$I^{(2)}_{(a,b)}(\omega,\lambda) = \sum_i \sum_j W_i W_j I^{(2)}_{(a,b)}(\omega,\lambda)|_{ij} \ , \tag{32}$$

where $I^{(2)}_{(a,b)}(\omega,\lambda)|_{ij}$ is the partial intensity emitted as a consequence of one interaction a on the atom Z_i, followed by one interaction b on the atom Z_j.

V. RESULTS AND DISCUSSION

A. Numerical methods

The intensities described by Eqs. (15), (24), (26), and (28) have been studied in pure elements of low and medium Z and in multicomponent mixtures [using Eq. (32)]. A Romberg integration algorithm generalized to improper integrals [38] was used for computing the innermost integrals in the Rayleigh-Rayleigh intensity and the single integrals in the other contributions with a precision of four figures. Significant differences of precision were found in Rayleigh-Compton and Compton-Rayleigh calculations between four- and five-figure accuracy, therefore five figures are recommended in this case. The outer integral (when it exists) is computed with a trapezoidal algorithm. Two meshes, 20 and 100 intervals, were tested to determine how important the density of the grid is. In all cases a lower density grid gave a comparable precision with $\frac{1}{5}$ of the computation time.

B. Calculations for pure targets

As follows from Eqs. (15), (24), (26), and (28), the intensities depend on some main physical variables: the atomic number Z of the scatterer, the incident wavelength λ_0, and the incidence and take-off beam directions.

The influence of Z is complex because it modifies a number of the problem variables: firstly, the scattering functions F and S; secondly, the attenuation coefficients μ of the target where the element Z can be a partial component. It is not easy to extract a general behavior since the attenuation coefficients are complicated functions of the energy and composition, as the scattering functions are, of the geometry and the energy. Figure 4 shows separately the behavior of the Compton intensity, the total double-scattering intensity under the Compton peak, and their ratio as a function of Z. The ratio vanishes for increasing Z, rendering a cleaner Compton peak in heavier elements. For low Z, double scattering can be high ($>70\%$ of the Compton peak for H) and, therefore, higher orders of multiple scattering should be calculated. Figure 5(a) shows double-scattering spectra for some elements of low and medium Z. The integrated intensity changes with constant energy width. The contribution of the partial double-scattering intensities relative to the total double-scattering intensity is strongly influenced by Z. In Fig. 5(b) it is shown how the Compton-Compton term decreases monotonically. The mixed-scattering Rayleigh-Compton and Compton-Rayleigh terms reach a maximum (near Al) and decrease with lower slope than the Compton-Compton term. The different slopes allow a similar contribution of the three components near Fe. For elements lighter than Fe the Compton-Compton intensity dominates. For heavier elements the mixed-component intensity become higher than the Compton-Compton intensity, their peaked shape producing a

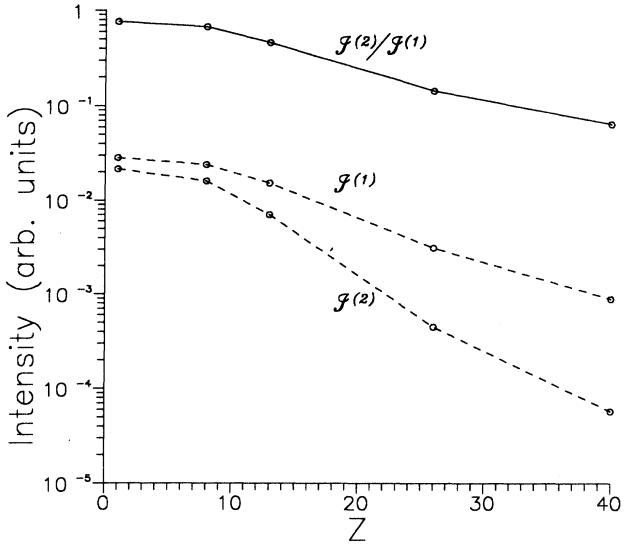

FIG. 4. The single- and double-scattering integrated intensities describing the overall contribution of the corresponding order of scattering. Here they are plotted as a function of the atomic number Z of the target for some representative elements (H,O,Al,Fe,Zr), polar angles of $\vartheta_0 = 45°$ and $\vartheta = 135°$ and an excitation of 59.54 keV. The double- to single-intensity ratio $\mathcal{J}^{(2)}/\mathcal{J}^{(1)}$ that gives the importance of the continuous second-order (Compton-Compton, Rayleigh-Compton, and Compton-Rayleigh) terms relative to the intensity of the Compton peak is plotted with a solid line.

greater distortion of the Compton profile.

The excitation energy E_0 (or wavelength λ_0) determines the position of the energy intervals for both the attenuation of the beam into the target and the next scattering. The attenuation is relevant in determining the relative importance of the contributions. It depends on a monochromatic energy for Rayleigh scattering, and extends along the width of the low-energy tail in the Compton case. When attenuation at E_0 predominates, the main contribution is the Rayleigh-Compton at low E_0 and the Compton-Rayleigh at high E_0. When attenuation at the tail energy (lower than E_0) prevails, the main contributions are Compton-Rayleigh at low E_0 and Rayleigh-Compton at high E_0. Figure 6(a) shows how the increase of E_0 has the effect of increasing the integral intensity without modifying the wavelength width (but

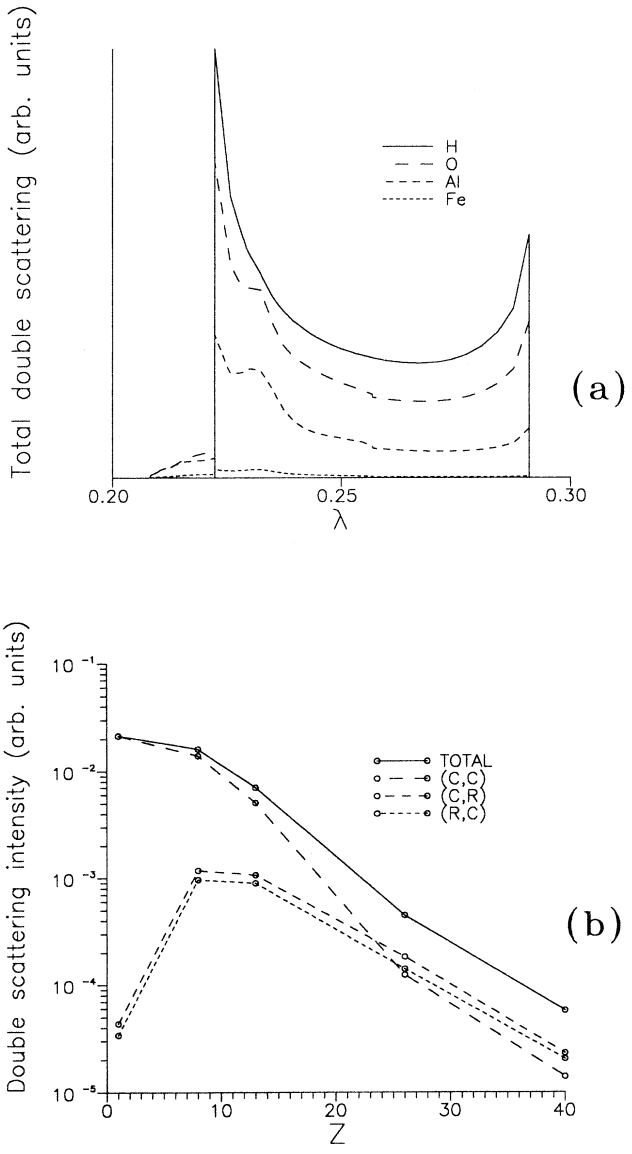

FIG. 5. (a) Total double-scattering wavelength spectra for some elements from H to Fe. The intensity of the double scattering is substantially greater for lighter elements. For heavier elements the Compton-Rayleigh and Rayleigh-Compton mixed contributions become more important. (b) Partial double-scattering intensities as a function of the atomic number Z. The Compton-Compton, Compton-Rayleigh, and Rayleigh-Compton continuous contributions are plotted as a dashed line. The total double scattering is plotted with a solid line. $\vartheta_0=45°$, $\vartheta=135°$, and the energy is 59.54 keV.

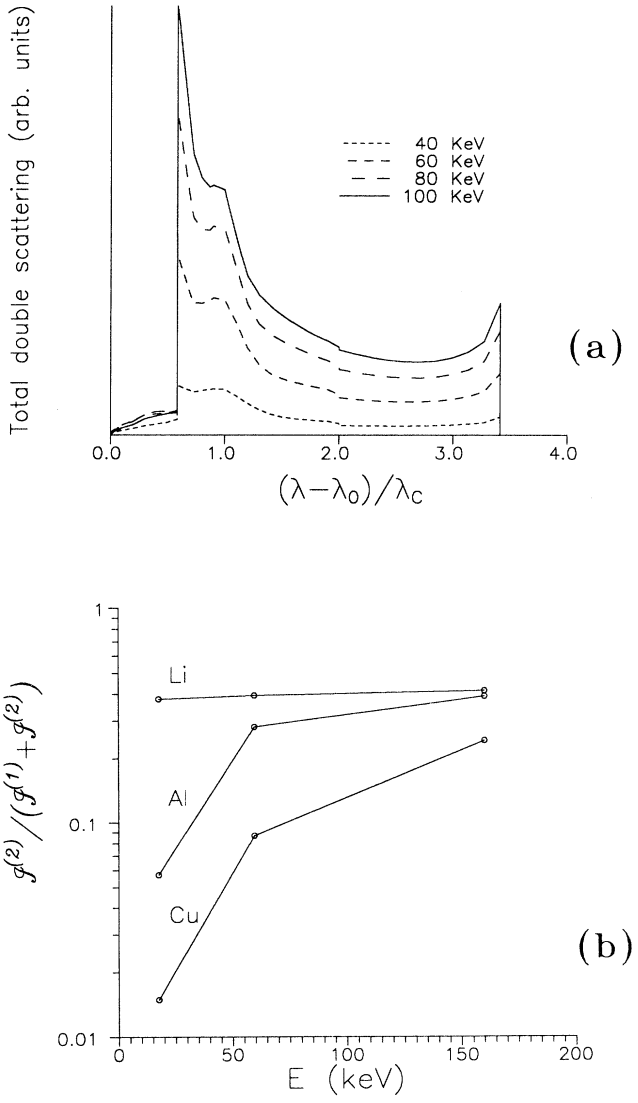

FIG. 6. (a) Total double scattering in Al as a function of the ratio $(\lambda-\lambda_0)/\lambda_C$ for several incidence energies E_0. The incidence and take-off angles are 45° and 135°, respectively. (b) The double scattering importance $\mathcal{R}_{\text{double}}$ for Li, Al, and Cu as a function of the incidence energy E_0. Three values of E_0 were used in the calculations (17.5, 60, and 160 keV) that approximately correspond to the energy of some excitation lines reported frequently in the literature (Mo $K\alpha$, ^{241}Am and ^{123}Tc). Incidence is normal and take-off is 150°. These values may be compared to Monte Carlo simulations performed in similar conditions (Ref. [42]).

shifting the wavelength origin) of the spectrum. In Fig. 6(b) we attempt to link the atomic number and the energy response for some representative elements. It is easily seen that the quantity $\mathcal{R}_{\text{double}}=\mathcal{J}^{(2)}/(\mathcal{J}^{(1)}+\mathcal{J}^{(2)})$ represents a lower limit for the multiple-scattering importance $\mathcal{R}=(\sum_{j>1}\mathcal{J}^{(j)})/(\mathcal{J}^{(1)}+\sum_{j>1}\mathcal{J}^{(j)})$. For the lowest Z $\mathcal{R}$ can be much more greater than $\mathcal{R}_{\text{double}}$ since higher-order scattering terms are important. For the rest of the Z, $\mathcal{R}_{\text{double}}$ can be considered as an acceptable (lower) estimation of $\mathcal{R}$. From this figure it is clear that multiple scattering becomes a very important fraction of the overall emission for increasing E_0 on all the elements exemplified. For low energies greater differences in the $\mathcal{R}$ importance arise for low Z.

The third important variable of the problem is the excitation-detection geometry. The influence of the geometry is not easy to analyze because of the difficulty of studying simultaneously the influence of the three angular variables ϑ, ϑ_0, and φ (assuming $\varphi_0\equiv 0$). The scattering angle χ (another important magnitude) can be defined in terms of these three angles. The angle χ defines the width of the continuous wavelength spectrum in the Compton-Compton case. A change in ϑ_0 and ϑ maintaining fixed χ varies the relative contribution of the partial second-order intensities to the double-scattering spectrum, and modifies the shape of the Compton-Compton intensity [see Fig. 7(a)]. Since χ is constant in this figure, the wavelength limits of the spectra remain unchanged. Figure 7(b) shows the behavior of the integrated intensities. The maximum of $\mathcal{J}^{(2)}/\mathcal{J}^{(1)}$ signals the worst peak-to-background figure. The best signal-to-noise ratios are obtained for ϑ_0 near 0° and 90°. The last value is preferable because of the higher intensity of the Compton peak.

The variation of the double-scattering spectra with ϑ_0 is shown in the example of Fig. 8(a). An increase of the polar angle ϑ_0 has the effect of changing the shape of the continuous spectrum, while it increases the integrated intensity. The signal-to-noise ratio has a similar behavior to that of the preceding case, with an improvement for ϑ_0 near 90° [see Fig. 8(b)]. Spectral shapes as a function of ϑ are shown in Fig. 9(a). The spectrum becomes narrower for increasing ϑ. The best signal-to-noise ratio is obtained in the neighborhood of 90° as shown in Fig. 9(b).

The effect of changing in a controlled way the scattering angle χ is shown in Fig. 10. The increase of χ produces the concentration of the spectrum at the energy of the Compton peak [Fig. 10(a)]. The $\mathcal{J}^{(2)}/\mathcal{J}^{(1)}$ ratio is displayed in Fig. 10(b). The best signal-to-noise ratio is obtained for small χ. The mot unfavorable situation corresponds to 90° scattering.

C. Comparison with experimental data

In order to compare the results of this theory with experimental data, a full spectrum for water was built by joining both the monochromatic and the multiple-scattering continuous parts. The first- and second-order contributions were calculated with the computer program SHAPE [21] using the analytical expressions deduced in this and preceding works. The third- and fourth-order components were determined with Monte Carlo simulation. The monochromatic peaks were artificially broadened with a Gaussian shape to improve the fit of the whole spectrum. The multiple-scattering orders are not retouched. The spectrum so obtained matches well experimental points as is shown in Fig. 11. As can be appreciated, multiple scattering introduces low deformation for this geometry.

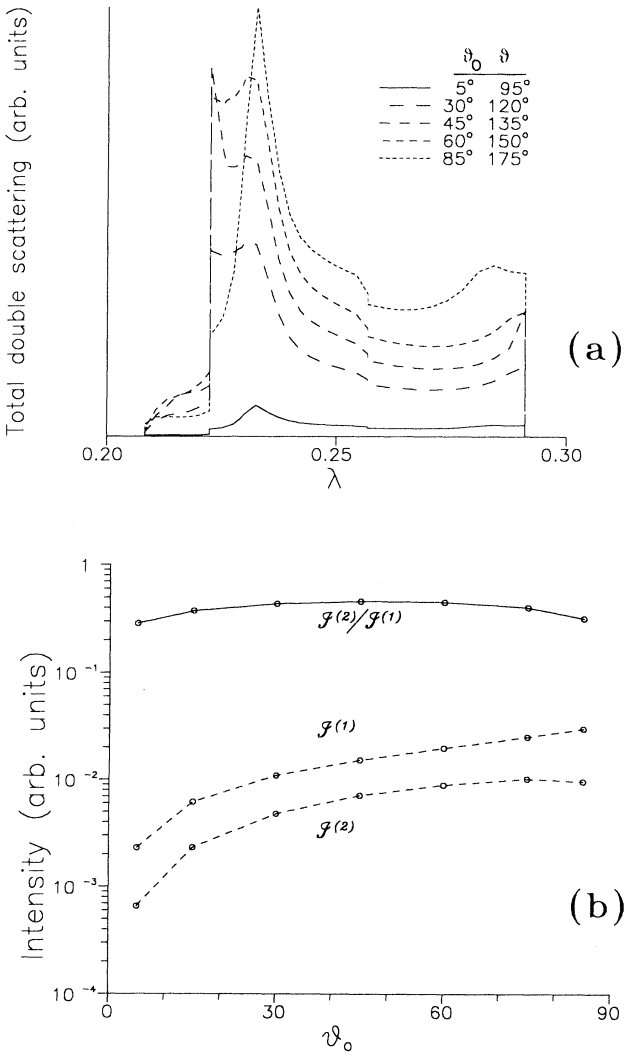

FIG. 7. (a) Double-scattering spectra of Al for a fixed scattering angle of 90° and $E_0=59.54$ keV. The incidence (take-off) polar angles are tilted in the scattering plane (maintaining χ unchanged) with values 5° (95°), 30° (120°), 45°(135°), 60° (150°), and 85° (175°), showing the change of the absorption for different geometrical situations. (b) Integrated intensities of single and double scattering as a function of the incidence polar angle for the cases explained above. With a solid line is plotted, in the same graph, the double- to single-intensity ratio which has a maximum near 45°.

VI. COMPARISON WITH OTHER WORK

The qualitative importance of multiple scattering has been estimated by many authors, but since it has been commonly applied to the correction of Compton profile measurements from slabs it makes implicit the dependence on the thickness of the target. Therefore it is not possible to make a straightforward comparison with published values of calculated intensities for infinite-thickness targets but rather with extrapolated points from the curves of intensity versus thickness found in the literature. Furthermore, these estimations were obtained by different means, ranging from analytical methods using different kind of approximations, to Monte Carlo simulations with several degrees of refinement. This variety makes it difficult to extract a unique representative set of data to compare to our results.

Our spectrum shape computations generally agree reasonably well with Monte Carlo simulations [39, 40] for reflection geometry, although those were performed for thin-thickness targets. In contrast, we do not agree with the Pitkanen *et al.* [40] assertion that the second-order distribution is bimodal for reflection geometry. Within the detail with which we have studied the second-order scattering there are three peaks well differentiated. Two of them belong to the extremes of the Compton-Compton

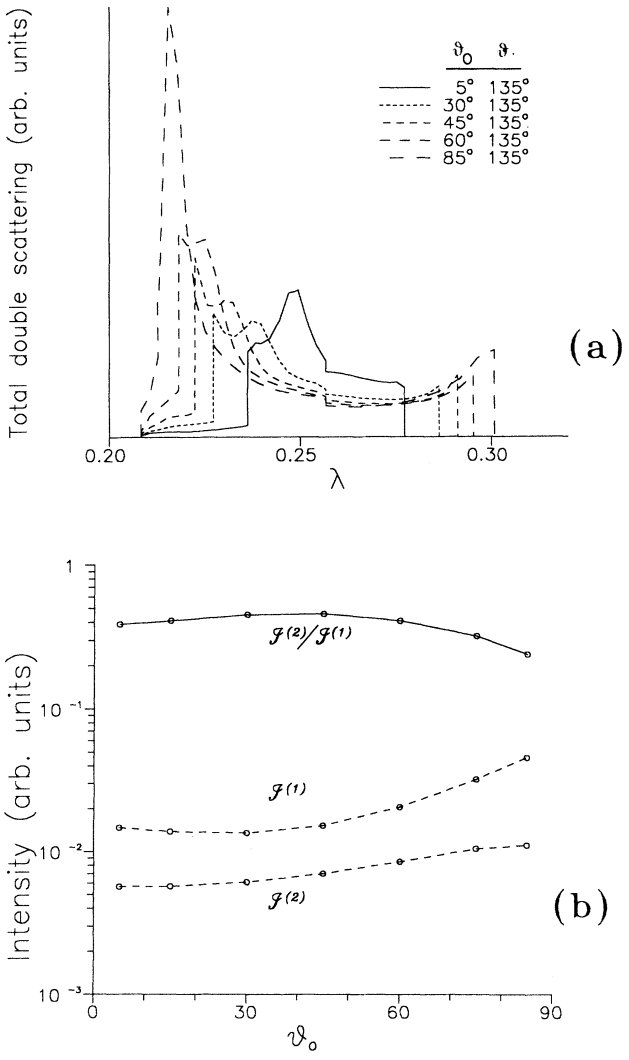

FIG. 8. (a) Total double-scattering spectra of Al, with fixed take-off angle of 135° and $E_0=59.54$ keV. The incidence polar angle is tilted in the same scattering angle plane with values 5°, 30°, 45°, 60°, and 85°. (b) Single and double scattering as a function of the incidence polar angle for Al, with fixed take-off polar angle of 135° and $E_0=59.54$ keV. The double- to single-intensity ratio is plotted in the same graph as a solid line.

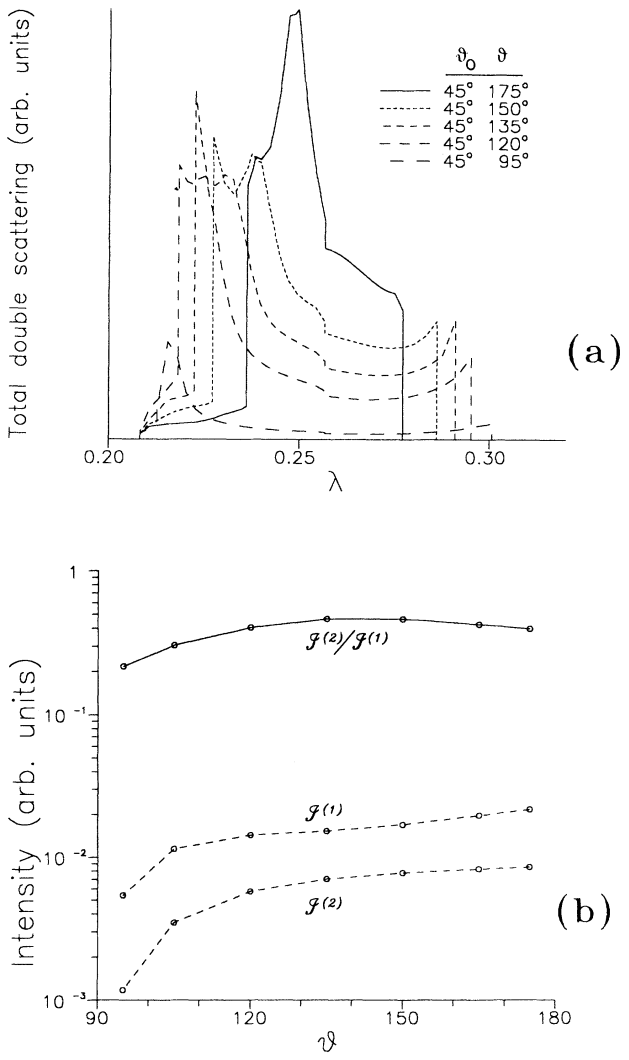

FIG. 9. (a) Total double-scattering spectra of Al, with fixed incidence polar angle of 45° and $E_0=59.54$ keV. The take-off polar angle is tilted in the same scattering plane with values 175°, 150°, 135°, 120°, and 95°. (b) Single and double scattering as a function of the take-off polar angle of Al, with fixed incidence polar angle of 45° and $E_0=59.54$ keV. The double- to single-intensity ratio is plotted in the same graph as a solid line.

distribution and the third one is the peaked distribution due to the sum of the Compton-Rayleigh plus the Rayleigh-Compton intensities whose maximum coincides with the Compton peak energy and which overlaps the peak. Furthermore, we also show that depending on the target, the excitation energy, and the geometry, the three peaks can look as two or still as only one.

In order to check independently our analytical results we performed a Monte Carlo simulation [41] with the same physical assumptions described along this work. The predicted Monte Carlo spectrum matches closely the analytical one, as it is shown in Fig. 12, except in the borders of the Compton-Compton spectrum where the analytical results can be better controlled than the Monte Carlo sampling. The three peaks can be clearly identified in the figure. We used the same Monte Carlo to explore the higher orders, and found that the multiple scattering with the pure Compton effect is the most important contribution in every case. We found another point of disagreement with the paper of Pitkanen *et al.* [40] regarding the amount of the third-order scattering. They estimated that contribution to be 10% of the second-order one, but as it is evident in Fig. 13 it can reach an entity much greater in light elements.

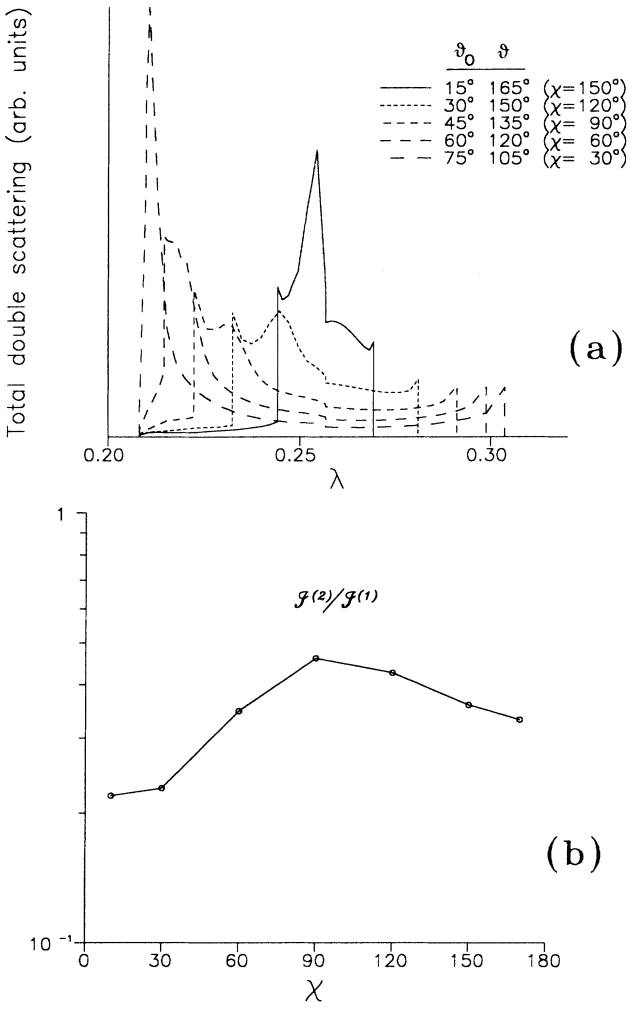

FIG. 10 (a) Total double-scattering spectra of Al for a fixed incidence energy of 59.54 keV. The polar incidence and take-off angles are changed in the same plane of scattering to obtain scattering angles of 30°, 60°, 90°, 120°, and 150°. The spectrum at 90° coincides with incidence and take-off angles of 45° and 135°, respectively. (b) Double- to single-intensity ratio as a function of the scattering angle χ. The incidence and take-off polar angles are assumed symmetrical about the normal to an Al surface. $E_0 = 59.54$ keV.

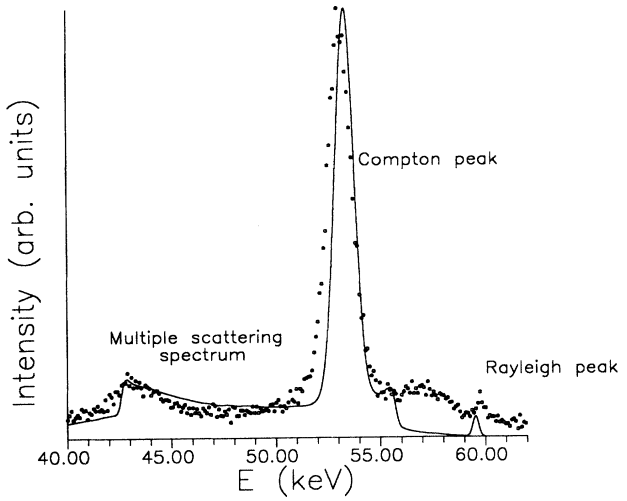

FIG. 11. X-ray spectrum of H_2O excited with the 59.54-keV line. The incidence and take-off angles are 45° and 135°, and $\varphi = \varphi_0 = 0°$. The solid line represents the theoretical estimation computed with SHAPE (Ref. [21]) and corrected with the third- and fourth-order interactions calculated with Monte Carlo simulation. Circles denote experimental data [courtesy of R. Sartori, FaMAF, University of Córdoba].

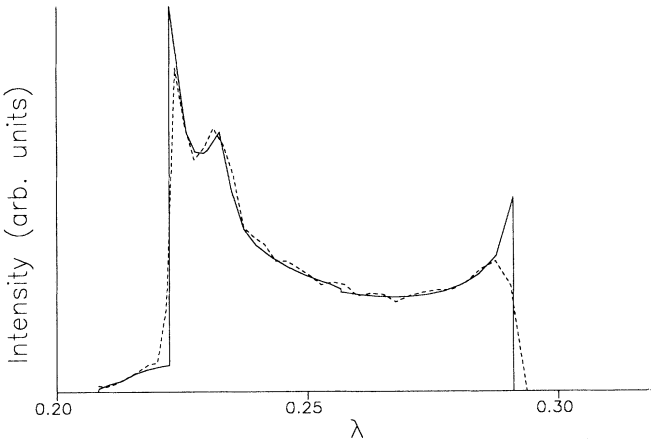

FIG. 12. Analytical prediction (solid line) of a second-order spectrum compared to a 50 000 histories Monte Carlo simulation (Ref. [41]) (dashed line) under the same conditions. The target is Al excited with 59.54 keV with $\vartheta_0 = 45°$, $\vartheta = 135°$, and $\varphi = \varphi_0 = 0°$.

Our results can also be compared to Monte Carlo predictions of the integrated intensity for the second-order scattering, or of the importance of the multiple-scattering intensity. Our data points in Fig. 6(b) can be confronted with infinite-thickness extrapolations to the curves in Fig. 1 of Felsteiner and Pattison [42]. Our results are consistent with their predictions for Al and Cu but not for Li, which they underestimated. We predict that the importance of multiple scattering for a thick target of Li must exceed the 30% threshold on all the three excitation energies they considered, even the lowest.

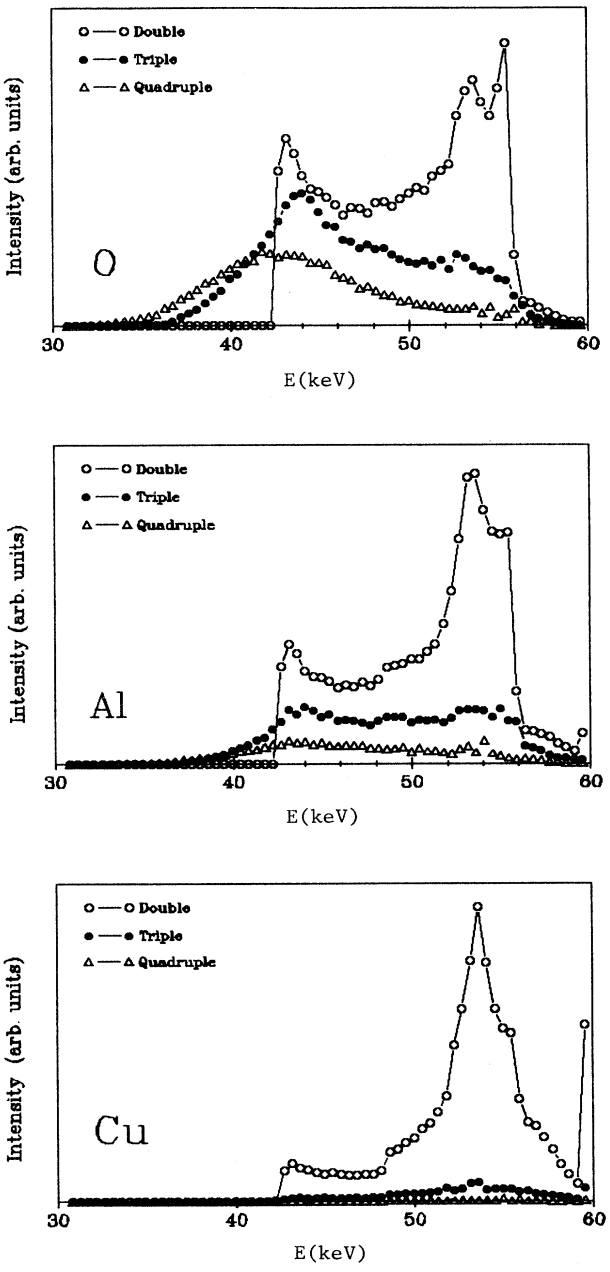

FIG. 13. Two-, three-, and four-collision total intensities simulated with Monte Carlo (Ref. [41]) for three elements excited with the same energy $E_0=59.54$ keV. Higher-order scattering becomes more important for light elements as can be appreciated (the heights of the plots are in scale 40:20:1 for increasing atomic number). Another element of quantification is the height of the coherent line (near the right side in the plots) that becomes more important for increasing Z. For low Z, third- and fourth-order contributions cannot be neglected.

VII. CONCLUSIONS

First of all, we have proved that the use of the transport theory is adequate to study single-order terms in problems of multiple interactions which fills a gap in the analytical approaches accepted to examine multiple-scattering corrections of Compton profiles.

The analytical expressions for the double-scattering intensities of the Compton and Rayleigh effects have been deduced using an order-of-interactions solution of the Boltzmann transport equation for unpolarized photons, already applied successfully to other atomic interactions in the x-ray regime. The relationships found describe the intensities contributed by every type of multiple interaction to the fluorescent x-ray beam as a function of the direction of incidence and of the incident beam energy. The target was assumed pure and homogeneous with infinite thickness, whose total attenuation coefficient depends on the Compton and Rayleigh scattering and the photoelectric effect. The Compton and Rayleigh interactions between unpolarized photons and stationary bound electrons were described with complete transport kernels including atomic scattering factors.

The four intensity contributions produced by double collisions of the Rayleigh and Compton effects were calculated, respectively, in Eqs. (15), (24), (26), and (28). These expressions plus the sum rule (32) are valid for computing the intensity emitted by a composite material.

The Rayleigh-Rayleigh contribution is the only discrete one. The others are continuous. The Compton-Rayleigh and Rayleigh-Compton spectra are peaked at the Compton wavelength and have equal widths of $\Delta\lambda=2\lambda_C$. The Compton-Compton distribution has a characteristic shape centered at $\lambda_0+2\lambda_C$ with peaks in the two extremes and DuMond's width $\Delta\lambda=4\lambda_C\cos(\chi/2)$. The three continuous contributions overlap and interfere with the unfolding of the Compton peak.

The double-scattering spectrum is defined by the overlap of the Compton-Compton, Rayleigh-Compton, and Compton-Rayleigh contributions. The shape of the spectrum has been studied as a function of the angular variables, the target material, and the energy E_0. All of these variables affect the shape of the spectrum in some way, either changing directly the width and the shape of the contributions, or modifying the relative probability of one interaction chain over the others, or changing the attenuation response of the material. The general behavior of the total intensity for double scattering can be summarized in the following points.

(a) It increases when the atomic number Z of the target decreases.

(b) It is greater when E_0 is greater.

(c) With increasing Z the relative importance of the mixed chains Compton-Rayleigh and Rayleigh-Compton increases over the Compton-Compton one. Therefore the spectrum concentrates under the main Compton peak increasing the deformation of the profile.

(d) The angular coordinates ϑ_0, ϑ, and $\varphi-\varphi_0$ (or the scattering angle χ) modifies strongly the shape of the spectrum, but a general behavior cannot be stated in a conclusive way.

The other important quantifier of the double-scattering behavior is the integrated intensity $\mathcal{I}^{(2)}$ expressed in units of $\mathcal{I}^{(1)}$, or in units of $\mathcal{I}^{(1)}+\mathcal{I}^{(2)}$. The first ratio gives the probability, relative to the main Compton peak, of the total double-scattering emission. It can also be interpreted as an estimation of the inverse signal-to-noise value. The second ratio, $\mathcal{R}_{\text{double}}$, defines a lower limit for the importance of the complete contribution of multiple scattering. Some other general conclusions can be derived from these magnitudes.

(e) The multiple-scattering contribution can be very important. For lighter elements it can easily exceed the 30% of the overall intensity on almost all the x-ray regime. For medium and high x-ray energies the multiple-scattering contribution exceeds 10% for all the elements of interest.

(f) The worst signal-to-noise values are obtained in the neighborhood of the configuration $\vartheta_0=45°$, $\vartheta=135°$, $\varphi=0°$, and $\varphi_0=0°$ ($\chi=90°$).

(g) The best signal-to-noise values are obtained for ϑ_0 and ϑ near 90°, and for χ near 0°.

As could be expected, the analytical computations match well the results of a Monte Carlo simulation based on the same physical assumptions. The same Monte Carlo was used to study the third and the fourth order. The importance of the higher orders is not negligible at all. The following general statement arises.

(h) The importance of the nth total contribution relative to the previous order $\mathcal{I}^{(n)}/\mathcal{I}^{(n-1)}$ can be approximated by the $\mathcal{I}^{(2)}/\mathcal{I}^{(1)}$ fraction. Therefore the nth contribution relative to the main Compton peak is given by $(\mathcal{I}^{(2)}/\mathcal{I}^{(1)})^{n-1}$.

The computed double-scattering spectrum, completed with the Monte Carlo simulated third- and fourth-order components and corrected by detector response, agree well with experimental data from nonpolarized x-ray sources.

Further work in this subject could be addressed to improving the knowledge of the higher-order terms of multiple scattering by means of this theoretical approach. The motion of the electrons and the polarization effects could only be considered at the price of reformulating completely the transport problem for which another solution should be found.

ACKNOWLEDGMENTS

I would like to thank Dr. Szabina Török of the Hungarian Academy of Sciences who attracted my attention to this problem, promoted stimulating discussions, and contributed her own experimental data in the first stages of this work. I would like to thank also Professor Marco Sumini for his interesting discussions on transport theory. Thanks are due to ENEA for supporting this research. I would also like to thank CONICET, Buenos Aires, for financial support.

*On leave from the Faculty of Mathematics, Astronomy and Physics, University of Córdoba, 5000 Córdoba, Argentina.

[1] *Compton Scattering: The Investigation of Electron Momentum Distributions,* edited by B. G. Williams (McGraw-Hill, London, 1977).
[2] M. J. Cooper, Rep. Prog. Phys. **48**, 415 (1985).
[3] W. Schülke, Nucl. Instrum. Methods A **280**, 338 (1989).
[4] V. Halonen, I. R. Epstein, A. C. Tanner, and B. G. Williams, in *Compton Scattering: The Investigation of Electron Momentum Distributions,* edited by B. G. Williams (McGraw-Hill, London, 1977), p. 79.
[5] J. W. M. Dumond, Phys. Rev. **36**, 1685 (1930).
[6] B. G. Williams, P. Pattison, and M. J. Cooper, Philos. Mag. **30**, 307 (1974).
[7] A. C. Tanner and I. R. Epstein, Phys. Rev. A **13**, 335 (1976).
[8] A. C. Tanner and I. R. Epstein, Phys. Rev. A **14**, 313 (1976).
[9] E. Braun-Keller and I. R. Epstein, Phys. Rev. A **16**, 1146 (1977).
[10] E. Braun-Keller and I. R. Epstein, Phys. Rev. A **16**, 1154 (1977).
[11] S. Chandrasekhar, Proc. R. Soc. London Ser. A **192**, 508 (1948).
[12] R. C. O'Rourke, Phys. Rev. **85**, 881 (1952); **89**, 999 (1953).
[13] P. J. Brockwell, Philos. Mag. **12**, 515 (1965).
[14] U. Fano, L. V. Spencer, and M. J. Berger, in *Neutrons and Related Gamma Ray Problems,* Handbuch der Physik Vol. 38/2, edited by S. Flügge (Springer, Berlin, 1960), p. 660.
[15] G. C. Pomraning, *The Equations of Radiation Hydrodynamics* (Pergamon, Oxford, 1973).
[16] J. E. Fernández, V. G. Molinari, and M. Sumini, Nucl. Instrum. Methods A **280**, 212 (1989).
[17] J. E. Fernández, X-Ray Spectrom. **18**, 271 (1989).
[18] J. E. Fernández, V. G. Molinari, and M. Sumini, in *Advances in X-Ray Analysis,* edited by C. S. Barrett *et al.* (Plenum, New York, 1990), Vol. 33, p. 553.
[19] J. E. Fernández and V. G. Molinari, in *Advances in X-Ray Analysis,* edited by C. S. Barrett *et al.* (Plenum, New York, 1990), Vol. 33, p. 573.
[20] J. E. Fernández, X-Ray Spectrom. (to be published).
[21] J. E. Fernández, and M. Sumini, X-Ray Spectrom. (to be published).
[22] J. H. Hubbell, W. H. McMaster, N. Kerr del Grande, and J. H. Mallett, in *International Tables for X-Ray Crystallography,* edited by J. A. Ibers and W. C. Hamilton (Kynoch, Birmingham, 1974), Vol. 4, p. 47.
[23] D. C. Creagh, Nucl. Instrum. Methods A **280**, 180 (1989).
[24] B. K. Agarwal, *X-Ray Spectroscopy* (Springer-Verlag, Ber-

lin, 1979).
[25] J. M. Jauch and F. Rohrlich, *The Theory of Photons and Electrons* (Springer-Verlag, Berlin, 1976).
[26] C. Bui and M. Milazzo, Nuovo Cimento D **11**, 655 (1989).
[27] N. G. Alexandropoulos, T. Chatzigeogiou, G. Evangelakis, M. J. Cooper, and S. Manninen, Nucl. Instrum. Methods A **271**, 543 (1988).
[28] D. E. Cullen, M. H. Chen, J. H. Hubbell, S. T. Perkins, E. F. Plechaty, J. A. Rathkopf, and J. H. Scofield, Lawrence Livermore National Laboratory, University of California, Report No. UCRL-50400, Vol. 6, Pts. A and B, Rev. 4, 1989 (unpublished).
[29] R. Ribberfors and K. F. Berggren, Phys. Rev. A **26**, 3325 (1982); **29**, 3451 (E) (1984).
[30] J. H. Hubell, W. J. Veigele, E. A. Briggs, R. T. Brown, D. T. Cromer, and R. J. Howerton, J. Phys. Chem. Ref. Data **4**, 471 (1975); **6**, 615 (E) (1977).
[31] J. H. Hubbell and I. Øverbø, J. Phys. Chem. Ref. Data **8**, 69 (1979).
[32] D. Schaupp, M. Schumacher, F. Smend, P. Rullhusen, and J. H. Hubbell, J. Phys. Chem. Ref. Data **12**, 467 (1983).
[33] W. J. Veigele, P. T. Tracy, and E. M. Henry, Am. J. Phys. **34**, 1116 (1966).
[34] D. T. Cromer and J. T. Waber, in *International Tables for X-Ray Crystallography,* edited by J. A. Ibers and W. C. Hamilton (Kynoch, Birmingham, 1974), Vol. 4, p. 71.
[35] O. Klein and Y. Nishina, Z. Phys. **52**, 853 (1929).
[36] R. D. Evans, in *Corpuscles and Radiation in Matter II,* Handbuch der Physik, Vol. 34, edited by S. Flügge (Springer, Berlin, 1958), p. 218.
[37] V. H. Smith Jr, A. J. Thakkar, and D. C. Chapman, Acta Crystallogr. A **31**, 391 (1975).
[38] W. H. Press, B. P. Flannery, S. A. Teukolsky, and W. T. Vetterling, *Numerical Recipes: The Art of Scientific Computing* (Cambridge University Press, Cambridge, 1986).
[39] J. Felsteiner, P. Pattison, and M. Cooper, Philos. Mag. **30**, 537 (1974).
[40] T. Pitkanen, D. Laundy, R. S. Holt, and M. J. Cooper, Nucl. Instrum. Methods A **251**, 536 (1986).
[41] R. Sartori and J. E. Fernández (unpublished).
[42] J. Felsteiner and P. Pattison, Nucl. Instrum. Methods **124**, 449 (1975).